ELSEVIER

Maritime aerosol optical thickness measured by handheld sun photometers

Kirk D. Knobelspiesse[a,b], Christophe Pietras[a,c], Giulietta S. Fargion[a,c], Menghua Wang[a,d,*], Robert Frouin[e], Mark A. Miller[f], Ajit Subramaniam[g], William M. Balch[h]

[a]*NASA Goddard Space Flight Center, Code 970.2, Greenbelt, MD, United States*
[b]*Science Systems and Applications, Inc., Greenbelt, MD, United States*
[c]*Science Applications International Corp., Greenbelt, MD, United States*
[d]*University of Maryland Baltimore County, Baltimore, MD, United States*
[e]*Scripps Institution of Oceanography, University of California, San Diego, La Jolla, CA, United States*
[f]*Brookhaven National Laboratory, Upton, NY, United States*
[g]*Earth System Science Interdisciplinary Center, University of Maryland, College Park, MD, United States*
[h]*Bigelow Laboratory for Ocean Sciences, West Boothbay Harbor, ME, United States*

Abstract

For several years, the NASA SIMBIOS Project has collected, processed, and archived optical aerosol data from shipboard sun photometers. The calibration, processing, quality control, and archival methodology for handheld sun photometers are described here, along with their deployment statistics. Data processing has been standardized for all instruments by using identical calibration methods, ancillary data, and processing software. Statistical analysis reveals a dataset influenced by its temporal and geographic distribution, while multimodal histograms for aerosol optical thickness (AOT) and Ångström exponent reveal varied aerosol populations. A K-means unsupervised classification technique is used to separate these populations. This separation is validated by showing individual classes are more likely to be log-normally (for AOTs) or normally (for Ångström exponents) distributed than the dataset as a whole. Properties for each class are presented, along with the characteristics of each class by regional oceanic basin. Results also compare favorably with maritime aerosols measured by land-based AERONET Cimels in island sites, while providing data coverage in previously sparsely sampled regions. Aerosol models employed by SeaWiFS (Sea-Viewing Wide Field-of-View Sensor) also compare favorably with these ground based measurements.
© 2004 Elsevier Inc. All rights reserved.

Keywords: Maritime aerosols; Ångström exponent; Aerosol optical thickness; Sun photometer

1. Introduction

Since 1997, the NASA Sensor Inter-comparison and Merger for Biological and Interdisciplinary Oceanic Studies (SIMBIOS) Project Office has maintained and deployed a pool of sun photometers for use in maritime regions. The SIMBIOS Project calibrates and maintains these instruments, while SIMBIOS Principal Investigators (PIs), at a number of institutions, deploy them on research cruises. Some SIMBIOS PIs also deploy their own instruments. The SIMBIOS Project then processes these data, performs quality control (QC), and archives the final result in the SeaWiFS Bio-Optical Archive and Storage System (SeaBASS) (Werdel and Bailey, 2002). SeaWiFS is Sea-Viewing Wide Field-of-View Sensor.

This paper is intended to be a macroscopic analysis of the entire dataset from two types of handheld sun photometers, each with five bands at visible and near-infrared (NIR) wavelengths. Data products from these instrument designs include aerosol optical thickness (AOT) at each wavelength

* Corresponding author. NASA Goddard Space Flight Center, University of Maryland Baltimore, Code 970.2, Greenbelt, MD 20771, United States. Tel.: +1 301 286 6421; fax: +1 301 286 0268.

E-mail addresses: kirk@simbios.gsfc.nasa.gov (K.D. Knobelspiesse), wang@simbios.gsfc.nasa.gov (M. Wang).

and the Ångström exponent computed from the AOT spectra. The nature of these handheld instruments is such that sky almucanters (a scan of sky radiance measurements made at the same zenith angle as the sun but varying azimuth angles), and thus aerosol particle size distributions, cannot be computed as it is for automated Cimel sun photometers deployed by the NASA Aerosol Robotic Network (AERO-NET) (Holben et al., 1998). However, our data can compli-

ment AERONET by sampling in previously inaccessible maritime regions. Calibration for the SIMBIOS Instrument Pool is achieved by comparing concurrent measurements between SIMBIOS and AERONET instruments at the AERONET rooftop facility at NASA's Goddard Space Flight Center in Greenbelt, MD.

The primary objective of the SIMBIOS Instrument Pool is to provide data for validation of aerosol products from
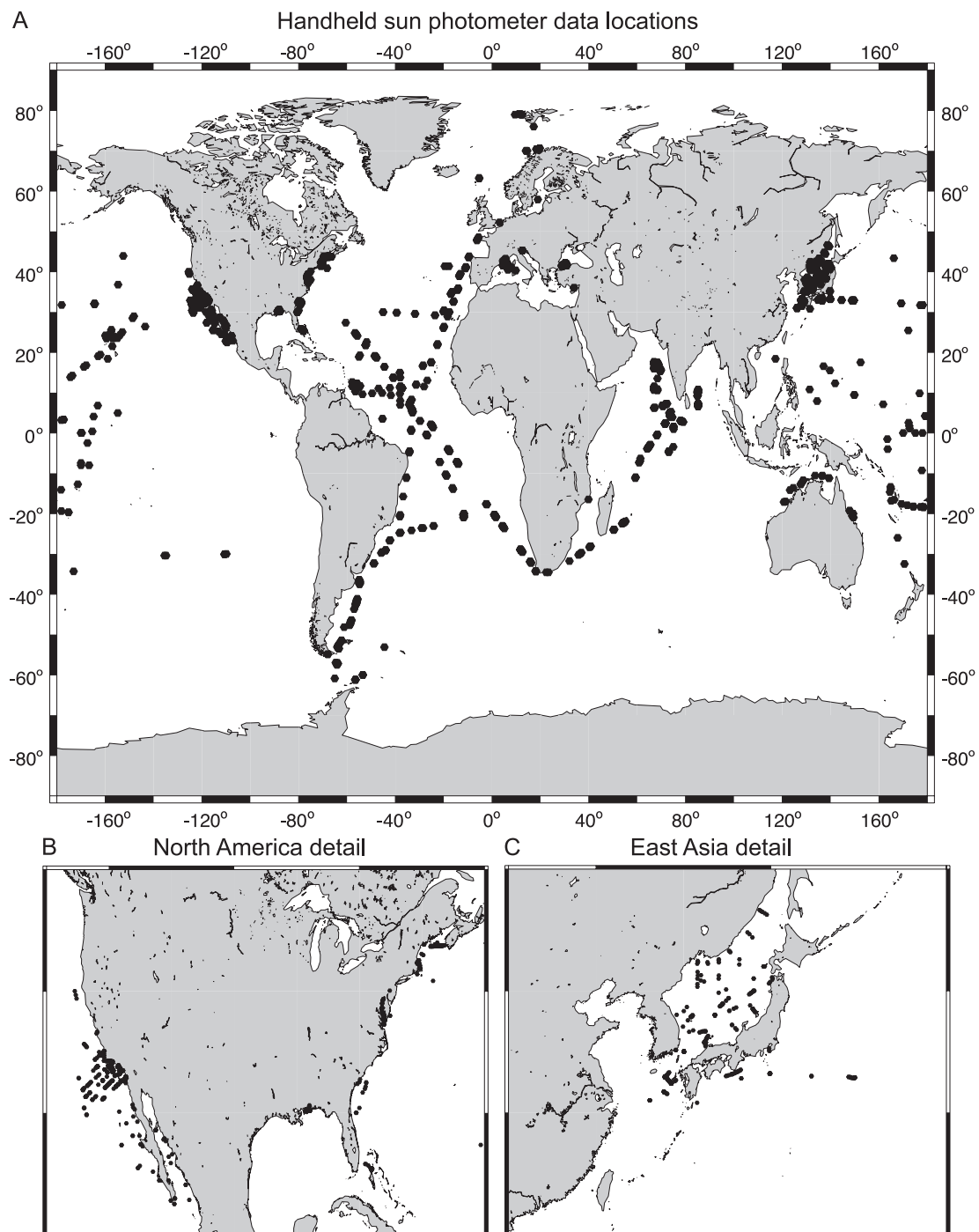

Fig. 1. Map of handheld sun photometer data locations. Part A shows the entire globe, while parts B and C show details in North America and East Asia, respectively.

SeaWiFS and other ocean color remote sensing satellites. The optical effect of aerosols upon the atmospheric correction of ocean color instruments is significant (Gordon & Wang, 1994). Comparisons of remotely sensed surface AOT from the SIMBIOS Instrument Pool to SeaWiFS AOT (a by-product of the atmospheric correction algorithm, Wang, 2000) can show the strengths and weaknesses of SeaWiFS atmospheric correction. This is particularly useful considering the volume of in situ bio-optical data gathered concurrently with aerosol data, providing the opportunity to validate other SeaWiFS (or other ocean color satellite) data products.

Surface measurements of column AOT can also be used to evaluate and refine aerosol models (Shettle & Fenn, 1979; Gordon & Wang, 1994) used in atmospheric correction. To do this, however, we must reduce the effects of data distribution upon dataset analysis. The SIMBIOS Instrument Pool was deployed on a variety of research cruises throughout the world's oceans. Heavily sampled regions include both East and West coasts of the United States and the Sea of Japan, as shown in Fig. 1. Data distribution is highly irregular, both temporally and geographically, so classification routines are utilized to split the data into groups of similar characteristics prior to analysis. This has paved the way to a proper comparison with data from AERONET and to SeaWiFS aerosol models.

2. Background

The SIMBIOS Instrument Pool contains several types of sun photometers, two of which form the basis of this study. The Microtops II Sun Photometer, commercially manufactured by Solar Light, is a five-channel, handheld, sun photometer whose collimated radiometers are pointed at the sun with the aid of a targeting device. The Microtops II Field of View (FOV) is 2.5 at full-width half maximum (FWHM), intended to be large enough to facilitate sun pointing without allowing significant sky-light into the collimators (Morys et al., 2001). The SIMBIOS Project owns 14 Microtops II's, which are deployed with external Global Positioning Satellite (GPS) units. The Simbad Radiometer is designed and manufactured by the Laboratorie d'Optique Atmospherique of the University of Lille, France. Like the Microtops II, the Simbad has five collimated radiometers and is pointed at the sun with the aid of a targeting device. It has a slightly larger FOV of 3.0° at FWHM and a built-in GPS unit. The Simbad also operates as an above water radiometer. It has two gain settings: a high gain for water radiometry and low gain for sun photometry. Simbad filters are also polarized to reduce the effect of surface reflection on measurements of water leaving radiance (Deschamps et al., 2004).

Both instruments are small, easy to use, and ideal for deployment in difficult situations like a ship at sea.

Ion deposition filters are used to provide stable bands with a width of about 10 nm. Table 1 shows the nominal center wavelengths of each sun photometer band. The Microtops II 940-nm band is intended for measurements of column integrated water vapor (WVC). SIMBIOS Project requirements do not include measurements of WVC, which need a more complicated instrument calibration (Ichoku et al., 2002). Therefore, AOT at 940 nm and WVC data are excluded from this study.

The Microtops II and Simbad sun photometers record data in internal memory, which are later downloaded by the PI to a text file that is forwarded to the SIMBIOS Project. Data are then processed and submitted to the SeaBASS database.

2.1. Sun photometry

The SIMBIOS Project uses handheld sun photometers because of their low cost, ease of calibration and operation, field hardiness, and ability of overcome difficulties associated with making optical measurements from a ship at sea. Handheld sun photometers are pointed at the sun to measure the spectral extinction of the direct solar radiation. This is expressed in the Beer–Lambert–Bouguer Law:

$$V(\lambda) = V_o(\lambda)\left(\frac{d_o}{d}\right)^2 e^{(-m\tau_t(\lambda))} \tag{1}$$

where:

$$\tau_t(\lambda) = \tau_a(\lambda) + \tau_R(\lambda) + \tau_g(\lambda) \tag{2}$$

Direct solar radiation is measured through filter bands with center wavelengths of λ and in terms of V, voltage. This signal is a function of the instrument's exo-atmospheric voltage, V_o, which expresses instrument calibration, d_o the average earth–sun distance, d the earth–sun distance on the day of observation, m the solar zenith angle-dependent airmass, and τ_t the total atmospheric optical depth. τ_t is the sum of the aerosol optical depth τ_a (AOT), the optical depth due to Rayleigh scattering τ_R, and optical depth due to gaseous absorption τ_g. In the visible to NIR wavelength range, gaseous absorption, τ_g, is mainly due to ozone. Instrument NIR wavelength sensitivity ranges were selected to avoid strongly absorbing water vapor features.

Table 1
Center wavelength

Instrument	Band center wavelength (nm)					
SIMBAD	443	490	560	670	870	
Microtops II	440	500		675	870	940[a]

[a] The 940-nm band is used for water vapor measurements and excluded from this study.

In our processing, d_o, d, and m are determined from the location and date of a particular measurement. The earth–sun distance ratio is calculated as (Iqbal, 1983):

$$\left(\frac{d_o}{d}\right)^2 = 1 + 0.034\cos\left(\frac{2\pi J}{365}\right) \tag{3}$$

where J is the Julian day of year. Airmass, m, is calculated according to Kasten and Young (1989):

$$m = \left(\cos\theta_o + 0.50572(96.07995 - \theta_o)^{-1.6364}\right)^{-1} \tag{4}$$

where θ_o is the solar zenith angle. The same airmass value is used for τ_t, τ_R, and τ_g, although Porter et al. (2001) and others suggest that m should be calculated individually. The effect is minor, so individual computations of m are not performed by the SIMBIOS Project.

τ_R is calculated using contemporary atmospheric pressure values provided by the National Centers for Environmental Prediction (NCEP). This relationship is:

$$\tau_R(\lambda) = \frac{P}{P_0} k_{Ray}(\lambda) e^{-\frac{H}{7998.9}} \tag{5}$$

where k_{Ray} is defined as

$$k_{Ray}(\lambda) = 28773.597886 \times \left[1 \times 10^{-8}\left(8342.13\right.\right.$$
$$\left.\left. + \frac{2406030}{130 - \lambda^{-2}} + \frac{15997}{38.9 - \lambda^{-2}}\right)\right]^2$$
$$\times \left[1 \times 10^{-8}\left(8342.13 + \frac{2406030}{130 - \lambda^{-2}}\right.\right.$$
$$\left.\left. + \frac{15997}{38.9 - \lambda^{-2}}\right) + 2\right]^2 \times \lambda^{-4} \tag{6}$$

In Eqs. (5) and (6), H is the altitude, in meters, above sea level, P is the atmospheric pressure, in millibars, and P_0 is the standard atmospheric pressure, with a value of 1013.25 mbar. Note that all wavelengths, λ, are in micrometers (Fargion et al., 2001).

Gaseous optical thickness, τ_g, is calculated using satellite observations of ozone. Preferably, ozone values from the Total Ozone Mapping Spectrometer (TOMS) are used. Data from the TIROS Operational Vertical Sounder (TOVS) are used when TOMS data are not available. If neither TOMS nor TOVS data exist for a particular time and location, ozone climatologies are implemented.

Optical thickness is computed from ozone using the relationship:

$$\tau_g(\lambda) = k_{oz}(\lambda)\frac{Z}{1000} \tag{7}$$

Z is the quantity of ozone, in Dobson units, and k_{oz} is the ozone absorption coefficient, shown in Table 2 (Nicolet, 1981; Komhyr et al., 1989).

Eq. (1), along with subsequent Eqs. (2)–(7) and ancillary ozone and pressure values, is used to solve for $\tau_a(\lambda)$ given $V(\lambda)$. $\tau_a(\lambda)$ values are therefore instrument-independent. In addition, ancillary pressure and ozone data are identical to those used in the SeaWiFS and many other ocean color satellites, adding confidence to the SIMBIOS Instrument Pool's value as a validation tool.

2.2. Calibration

The cross calibration technique consists of making near simultaneous direct solar measurements with two sun photometers. One sun photometer is a master instrument whose responsivity is well known. The second sun photometer is an uncalibrated instrument that requires a calibration transfer. A rooftop facility operated by the AERONET group at Goddard Space Flight Center (GSFC) is used to cross calibrate the sun photometers that compose that project's network of automatic instruments deployed around the world (Holben et al., 1998). The same facility is used to cross calibrate SIMBIOS sun photometers.

Master sun photometers are calibrated with the Langley technique in high-altitude (3400 m) conditions at Mauna Loa Observatory (MLO) by the AERONET group and then deployed at GSFC. Master instruments are calibrated on a 3-month cycle to ensure that one or two MLO calibrated instruments are always operating on the rooftop facility. AERONET master instruments have a spectrally dependent (highest at shortest wavelengths) AOT uncertainty of ~0.002–0.009 (Eck et al., 1999).

Exo-atmospheric voltages from the uncalibrated sun photometer are calculated relative to the ratio of the voltages from the master sun photometer:

$$V_o(\lambda) = \frac{V_o'(\lambda)V(\lambda)}{V'(\lambda)} \tag{8}$$

where $V_o'(\lambda)$ is the exo-atmospheric voltage for the master sun photometer, and $V(\lambda)$ and $V'(\lambda)$ are the signals measured by the uncalibrated and the master sun photometers, respectively.

Table 2
k_{oz} spectral dependence

Wavelength	440	443	490	500	560	670	675	870
k_{oz}	0.0034	0.0038	0.0223	0.0328	0.1044	0.0449	0.0414	0.0036

Some instruments have slightly different band center wavelengths than those in the master instrument. The closest channel, λ_j, to the uncalibrated instrument band center, λ_i, is used in calculations that are adjusted to account for differences in Rayleigh scattering, ozone absorption and the aerosol extinction:

$$V_0(\lambda_i) = \left[\frac{V_0{}'\left(\lambda_j\right) V(\lambda_i)}{V'\left(\lambda_j\right)} \right] e^{m\phi} \qquad (9)$$

where m is the airmass and ϕ is computed:

$$\phi = \tau_R(\lambda_i) - \tau_R\left(\lambda_j\right) + \tau_g(\lambda_i) - \tau_g\left(\lambda_j\right) + \tau_{a0}\left(\lambda_i{}^{-\alpha} - \lambda_j{}^{-\alpha}\right) \qquad (10)$$

τ_R is the Rayleigh optical thickness, τ_g is the ozone optical thickness, τ_{a0} is the aerosol optical thickness at 1 μm, and α is the Ångström exponent from Section 2.4.1. Both τ_{a0} and α are from the master instrument, where τ_{a0} is estimated by extrapolating shorter wavelength values of τ using α.

Exo-atmospheric voltages are calculated for pairs of measurements between the uncalibrated and the master sun photometers, usually taken within 30 s, though occasionally a time difference of 60 s is used to increase the number of matches. Only measurements for airmasses (m) less than 3 are used to avoid long atmospheric optical paths, which increases the possibility of encountering variable aerosol types. Computed exo-atmospheric voltages for the uncalibrated instrument are then averaged and the variability is checked. If the coefficient of variation is less than one percent, cross calibration is deemed a success.

2.3. Data collection, protocols

The SIMBIOS Project has established a strict set of protocols to ensure uniform and appropriate measurements for all data (Fargon & MacClain, 2003; Fargion & Mueller, 2000, Mueller & Fargon, 2002a, 2002b; Mueller et al., 2003a, 2003b, 2003c). PIs make measurements at each cruise station (where the research ship stops to collect water samples and other information) and during satellite overpass of relevant ocean color sensors such as SeaWiFS (local noon overpass). If time permits, additional measurements are made while the ship is underway. To account for Microtops II detector temperature-dependence, that instrument's power is cycled prior to each set of measurements. The Microtops II records the dark current voltage when turned on, and this value is subtracted from the instrument voltage, $V(\lambda)$, in Eq. (1), thus removing the instrument's temperature dependence (Porter et al., 2001). The Simbad can make manual measurements of the dark current, so it is left on continuously to ensure the detectors remain stable.

Both instruments are used only when the sky is clear of clouds at least 30 from the sun. Special attention must be made to ensure that thin layers of cirrus clouds are not in the optical path, as their cloud optical thickness can be confused as AOT. Several subsequent measurements (typically about 15, over an interval of about 5 min) of AOT are taken at each site, so that data stability can be analyzed, and used in pointing error screening routines (see Section 2.3.1). While at sea, optical surfaces are cleaned regularly to remove salt and dust deposits. Finally, data are downloaded and archived on a daily basis for redundancy.

2.3.1. Pointing error screening

Porter et al. (2001) noted that measurements from the Microtops II sun photometer can be biased when used at sea. This is due to the difficulty pointing the instrument at the sun accurately, with the result of missing the full solar signal. This causes a decrease in $V(\lambda)$ and an increase in $\tau_a(\lambda)$, often non-uniformly across bands. Both Microtops II and Simbad instruments sample $V(\lambda)$ several times for each data point, saving the highest, or average of the highest, $V(\lambda)$ values to a file. For the Microtops II, this is not sufficient for measurements taken in adverse sea conditions. For that instrument, a second screening algorithm is applied after the experiment to remove sun pointing errors. This algorithm examines each set of measurements, and iteratively removes high $\tau_a(\lambda)$ values until the coefficient of variation (CoV) of the set falls beneath a threshold (Knobelspiesse et al., 2003). The screening algorithm is not used for the Simbad because that instrument has a higher measurement frequency and an internal pointing error screening algorithm that is successful at sea.

2.4. Uncertainty computation

An uncertainty analysis of SIMBIOS sun photometers was recently performed, so individual values for AOT and Ångström exponent uncertainty are computed for each measurement and archived with the rest of the data. The Microtops II uncertainty calculation is done according to Russell et al. (1993) and Eck et al.(1999), and is written:

$$\delta_{\tau_a} = \left[\left(\tau \frac{\delta m}{m} \right)^2 + \left(\frac{\delta V_0}{m V_0} \right)^2 + \left(\frac{\delta V}{m V} \right)^2 + \left(\frac{\delta \tau_R}{\tau_R} \right)^2 + \left(\frac{\delta \tau_g}{\tau_g} \right)^2 \right]^{1/2} \qquad (11)$$

where $\delta \tau_a$ is the one sigma AOT uncertainty, δm is the airmass uncertainty, with a value of 0.001, δV_0 is the calibration coefficient uncertainty, with a value of 0.015 when V_0 is computed by a cross-calibration with AERONET instruments (see Section 2.2 and Eck et al., 1999), δV is the instrument voltage uncertainty, at 0.01, $\delta \tau_R$ is the uncertainty of the Rayleigh optical thickness, with a value of 0.005, and $\delta \tau_g$ is the uncertainty of the ozone optical thickness, with a value of 0.0045. Eq. (11) shows that AOT uncertainty is slightly proportional to total optical thickness,

Table 3
Sun photometer uncertainties

Wavelength (nm)	443/440	490/500	560	670/675	870
SIMBAD $\delta\tau_a$	0.021	0.020	0.018	0.011	0.010
Microtops II $\delta\tau_a$	0.015	0.015	–	0.015	0.015

while inversely proportional to airmass. Typical Microtops II $\delta\tau_a$ values are presented in 3. Simbad uncertainties are described in Deschamps et al. (2004) and presented in Table 3.

More information about the SIMBIOS Instrument Pool uncertainty analysis can be found in Fargion and McClain (2003).

2.4.1. Ångström Exponent calculation

The Ångström exponent is a parameter derived from multiple bands of AOT data to express the spectral nature of those bands, and thus information about the size distribution of the aerosol particles (O'Neill & Royer, 1993). It is defined by the Ångström Law (Ångström, 1929), shown in Eq. (12):

$$\tau_a(\lambda) = \tau_{a0}\lambda^{-\alpha} \tag{12}$$

where α is the Ångström exponent, $\tau_a(\lambda)$ is the AOT for wavelength λ, and τ_{a0} is the AOT at 1 µm.

The Ångström exponent is often calculated by determining the slope of a linear fit to the logarithm of λ vs. the logarithm of τ_a. For two bands, this is expressed in Eq. (13):

$$\alpha = \frac{\ln[\tau_a(\lambda_2)] - \ln[\tau_a(\lambda_1)]}{\ln(\lambda_1) - \ln(\lambda_2)}. \tag{13}$$

From an operational point of view, the above approach can yield different values of α when used with different combinations of λ_1 and λ_2 if α is not purely constant with respect to wavelength or τ_a is affected by noise (Eck et al., 1999).

The SIMBIOS Project uses sun photometers with a variety of different spectral bands, each with unique uncertainty values. As such, an Ångström exponent computational method was established that is less vulnerable to varying combinations of λ, minimizes noise in τ_a, and provides an uncertainty value for the result. This approach uses a non-linear, least squares, iterative fit of all available optical values between 440 and 870 nm of τ_a to Eq. (12). Individual values of τ_a in this fit are weighted by their uncertainty, and the α result has an uncertainty associated with that of the corresponding τ_a's.

Extremely unreasonable Ångström exponents, and Ångström exponents with large uncertainties, were removed from the SIMBIOS instrument dataset. α was restricted to within -1.0 and 3.0, values intended to encompass the greatest potential geophysical range and avoid masking instrumental or calibration errors which could result in an α bias. This restriction is intended to remove α values that are unreasonable due to τ_a noise. Further noisy τ_a screening is achieved by removing Ångström exponents whose uncertainty does not abide by the following empirical relationship:

$$\Delta\alpha < 2\alpha + 0.5 \tag{14}$$

The basis for the above equation comes from a semi-empirical analysis of the relationship between τ_a noise and Ångström exponent uncertainty illustrated in Fig. A.1, and is intended to only remove Ångström exponents derived from extremely noisy τ_a's. Data whose Ångström exponents are outside the reasonable range or whose Ångström exponent uncertainty does not fit Eq. (14) are marked as

Table 4
Quality control tests

Visualization type	Purpose	Action taken if error
Map of data locations	to determine if GPS is working properly	remove/modify location if data is over land or clearly not in the cruise region
Text file with data statistics	to confirm data are within reasonable bounds	investigate source file and processing routines for errors
Data histogram plots	to confirm data are within reasonable bounds	investigate source file and processing routines for errors
Plot of calibration coefficient (V_0) time sequence	to determine if calibration coefficients were used properly and if the instrument is temporally stable	investigate if calibration coefficient processing was correct, possibly replace instrument filters or detectors
Time sequence plot of both screened and unscreened τ_a (500 nm) values	to confirm data are within reasonable bounds and that the pointing and cloud screening routines worked properly	investigate source file and processing routines for errors, notify PI if measurement protocol was incorrect
Time sequence plot of both screened and unscreened Ångström exponent values	to confirm data are within reasonable bounds and that the pointing and cloud screening routines worked properly	investigate source file and processing routines for errors, notify PI if measurement protocol as incorrect

'missing'. AOT values for the same data point are not removed. More details about Ångström exponent computation and an analysis of the relationship between τ_a and Ångström exponent uncertainty are in Appendix A.

2.5. Quality control

Following processing, a number of plots, maps, and other data visualizations are created for each file. These are used to perform QC to ensure data fall within reasonable bounds of time, date, location, and value. The plots are also archived in SeaBASS for future use (Werdell & Bailey, 2002). Table 4 lists the various visualizations, their purpose, and the actions taken when problems are found.

If a particular file passes all the above QC tests, it is ingested into the SeaBASS database and archived. All data in this analysis passed QC tests.

3. Entire dataset analysis

The SIMBIOS Project has been collecting and archiving remotely sensed, surface sun photometer aerosol data since 1997. While this has involved a variety of sun photometer designs, this analysis is restricted to the Microtops II and Simbad sun photometers, due to the frequency of their measurements, similar nature of their designs, and confidence with their calibration, processing, QC, and uncertainty analysis. This dataset represents the final versions of all Microtops II and Simbad files archived in SeaBASS as of May 2003. It consists of 102 Microtops II and 46 Simbad files, representing 34 experiments and 145 individual cruises (see Table D). The dataset contains nearly 11,000 individual data points, about 4800 of which were taken with the Microtops II and 5900 with the Simbad. These measurements were made in a variety of atmospheric conditions and represent several aerosol types. Due to the temporally and geographically irregular nature of these
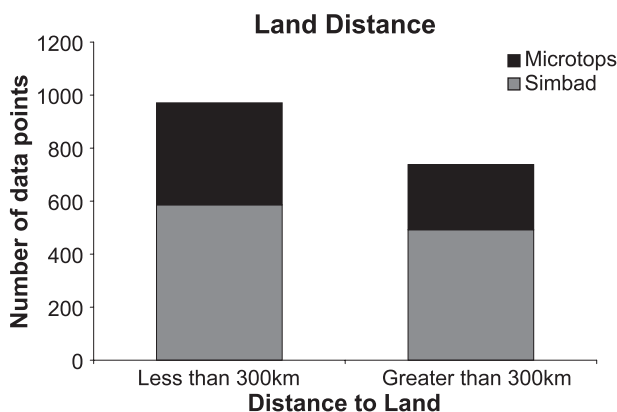
Table 5
Entire dataset statistics

All handheld data, 1709 data points

Parameter	Mean	Median	STD	Skewness	Kurtosis
AOT 440 nm	0.22	0.14	0.20	2.0	5.4
AOT 443 nm	0.22	0.14	0.20	2.0	5.5
AOT 490 nm	0.20	0.13	0.19	2.1	6.7
AOT 500 nm	0.20	0.12	0.19	2.2	6.8
AOT 560 nm	0.18	0.11	0.18	2.4	8.5
AOT 670 nm	0.15	0.09	0.16	2.8	12.
AOT 675 nm	0.15	0.09	0.16	2.8	12.
AOT 870 nm	0.13	0.08	0.15	3.3	16.
Ångström exponent	0.87	0.97	0.65	0.0	−0.3
Land distance	580	220			

data, much of the scientific benefit requires splitting data into sections representing the different aerosol populations. Before that can be done, however, a statistical analysis of the entire data set can be useful to establish the nature of the data and its underlying processing routines.

The Microtops II and Simbad radiometers utilize different sets of filters and thus have varying band center wavelengths. To account for this, an interpolation routine was utilized to compute AOT for common bands. This interpolation uses the spectral AOT, Ångström exponent, and associated uncertainties to determine an AOT and uncertainty for common bands. For the purposes of classification (see below), Simbad AOT values were interpolated to an AOT at 500 nm.

3.1. Binning

In an attempt to further reduce the sampling effect on the data, we have binned it into half hour segments with near similar location. For AOT data, binning utilizes the geometric mean, which is most appropriate for log-normally distributed data (Campbell, 1995). Arithmetic means were used for the normally distributed Ångström exponent. Binning reduced the number of individual data points from 10,787 to 1715, indicating that a considerable portion of the original data were captured in groups and are perhaps redundant. To test binning validity, statistics of the binned data were compared to the same for the original data. Binned AOT median values are nearly unchanged (as can be expected for log-normally distributed data), while the binned mean Ångström exponent value has not changed. We can therefore conclude that data binning has reduced redundant data while preserving its statistical characteristics.

3.2. Basic statistics

Most of the aerosol data collected by the SIMBIOS Project was gathered along with other bio-optical data, such as profiles of apparent and inherent water optical properties and phytoplankton pigment concentrations. Typically, mea-

Fig. 2. Distance to land histogram. Distance to major landmasses were computed for each global 1×1° region.
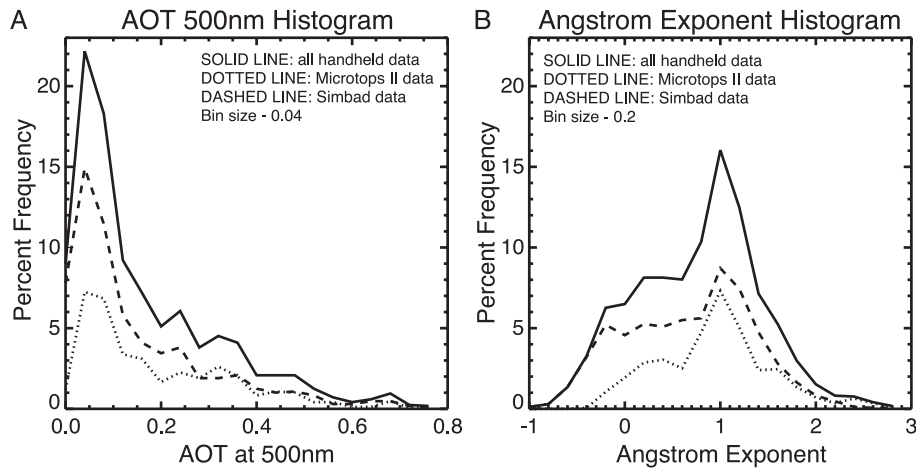
Fig. 3. Histograms of AOT at 500 nm (A) and Ångström exponent (B) for the entire (solid line), Microtops II (dotted line) and SIMBAD (dashed line) data sets. Bin sizes used in histogram computation were 0.04 for AOT at 500 nm and 0.2 for Ångström exponent.

surements are made as part of a larger experiment and/or research cruise (Mueller et al., 2003a). While this can be quite useful to fully understand the radiative transfer of a particular scene, time, or region, analysis of the entire dataset is influenced by the particular temporal and spatial data distribution. Indeed, Figs. 1 and 2 show that data sampling favors coastal regions, particularly the continental United States and East Asia. Distance to shore, as shown in Fig. 2, is a rough calculation of distance to major landmasses for each degree latitude/longitude box (see Section 3.3). In subsequent sections of this paper, we attempt to account for the irregularity in our distribution by splitting the data into groups of similar data representing various aerosol species.

Table 5 contains various statistical parameters describing the aerosol data set. For the AOT values, differences between mean and medians indicate that the data are not normally distributed or represent several different populations. Positive

skewness and kurtosis further establish the existence of non-normal distribution, indicating that most outliers are larger than the mean (positive skewness) and that the histogram has a leptokurtic (sharply peaked) nature (positive kurtosis) (Sokal & Rohlf, 1995). The severity of this skewness and kurtosis increases with AOT wavelength. We intend to show that AOTs, by nature, are log-normally distributed. Fig. 3A is the histogram of AOT at 500 nm. While the histogram is clearly more similar to a log-normal than a normal distribution, its multiple peaks and generally irregular nature suggest the data are composed of several populations representing different aerosol species. This is reinforced in the histogram of the Ångström exponent (Fig. 3B) and in Table 5. The Ångström exponent is derived from ratios of AOT at different bands (Section 2.4.1), so we would expect it to be normally distributed if the data were from a single population. However, mean and median values differ, and the kurtosis is non-zero. Therefore, the data must be split
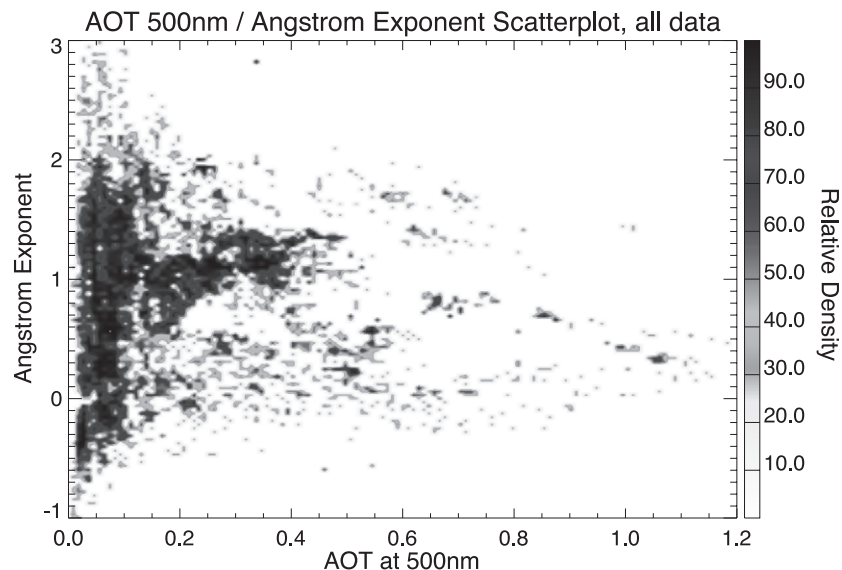

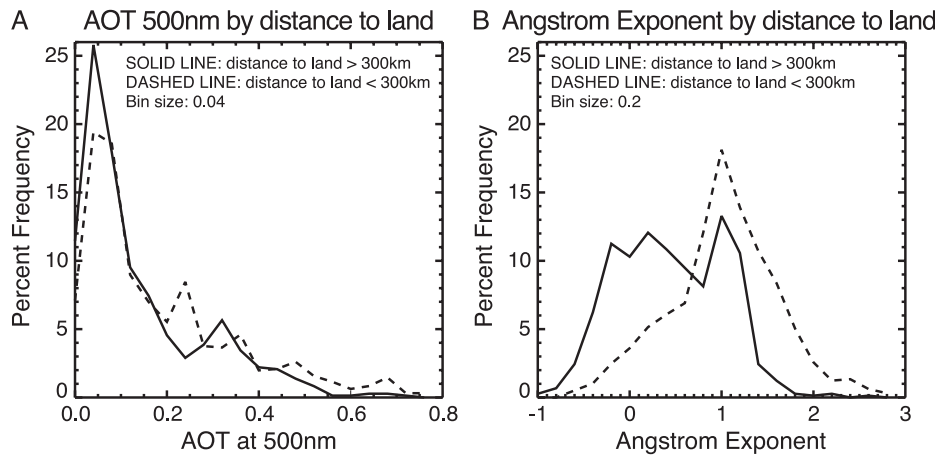Fig. 4. Two-dimensional histograms of aerosol optical thickness at 500 nm versus Ångström exponent.

Fig. 5. Histograms of data split by distance to land. Solid lines represent data measured within 300 km of a major landmass, while dashed lines represent data at least 300 km from shore.

into component aerosol species prior making any statistical conclusions about nature of maritime aerosols.

Fig. 4 is a scatter plot of AOT at 500 nm vs. Ångström exponent, illustrating the different aerosol specie present in the data. The Ångström exponent value is related to aerosol particle size (O'Neill & Royer, 1993), so aerosol type can be inferred by location on a scatter-plot like this. Data clusters indicate the presence of a specific aerosol type. The scatter plot shows wind-driven maritime and continental dust aerosols, which can be found in oceanic regions far from shore. They tend to have large particle sizes, and thus small Ångström exponents. Maritime aerosols typically have low optical thicknesses, so data with Ångström exponents less than about 1.0 and AOT values less than about 0.15 can generally be attributed to maritime aerosols (Smirnov et al., 2003). Dust typically has large particle size and large optical thicknesses, so the widely scattered data with AOT values greater than 0.15 could be attributed to dust. In our data classification (see Section 4), we attempt to identify these two types of aerosols, as they are important for our Ocean Color satellite atmospheric correction. Other non-dust continental aerosols, from sources such as urban pollution or biomass burning, are not modeled as completely in SeaWiFS (they are more difficult to determine with the available spectral sensitivity). Although they are important for SeaWiFS atmospheric correction, they are difficult to validate. These non-dust continental aerosols tend to be closer to land and more optically complex. While Fig. 4 shows several distinct data clusters for these high (greater than 1.0) Ångström exponent aerosols, our subsequent classification groups them into one class, as these aerosols are not typically modeled in ocean color atmospheric correction.

Of course, these boundaries are purely empirical, and Fig. 4 shows many cases where the type of aerosol is ambiguous. This could be the result of several factors, including higher Ångström exponent uncertainties as AOT decreases and complex vertical aerosol distributions. Section 4 is devoted to dividing the data into species in a more

elegant nature that utilizes iterative classification routines and geographical data.

3.3. Geographic data dependency

Geographic location can be a useful metric to help assess the type and origin of the aerosol measured by a particular data point. However, this quickly becomes complicated when dealing with thousands of measurements throughout the entire globe. In an effort to simplify this process, we added a field to our data that expresses the distance to the nearest large landmass. Land distance is not an exclusive way of determining aerosol type, as it neglects wind direction and other aerosol circulation factors, is subject to differences in source landmass, and is based upon a rather arbitrary determination of what constitutes a 'large land-mass'. Despite this, land distance, when used in conjunction with other aerosol parameters, can be useful when attempting to split the data into separate aerosol species. Land distance was computed by creating a global map of distance to nearest large landmass for each point within a latitude and longitude degree grid.

In an effort to demonstrate the significance of land distance upon aerosol parameters, the SIMBIOS Instrument Pool was split into two groups. The first, called the 'coastal' class, consists of data within 300 km of a major landmass. The 'offshore' class is all the data captured at least 300 km

Table 6
Data split by major landmass distance

Parameter	Mean	Median	STD
Coastal: x≤300 km, 971 data points			
AOT 500 nm	0.21	0.14	0.20
AOT 870 nm	0.13	0.07	0.16
Ångström exponent	1.1	1.1	0.60
Offshore: x>300 km, 738 data points			
AOT 500 nm	0.18	0.10	0.17
AOT 870 nm	0.13	0.09	0.14
Ångström exponent	0.55	0.52	0.58

Table 7
Class center boundaries

Class	τ_a min	τ_a max	α min	α max	Subclasses	Data points
Class 1—dust	0.2	1.50	−0.5	0.8	5	237
Class 2—maritime	0.00	0.15	−1.0	0.9	14	592
Class 3—non-dust continental[a]	–	–	–	–	16	886

[a] Class 3 represents all previously ungrouped data and is not constrained by class center.

from a major landmass. Selection of 300 km as the divider between coastal and offshore regions is arbitrary, but sufficient to illustrate the differences between data close to and far from land. Fig. 2 is the histogram for the quantity of data in each class. Histograms of the data products themselves are shown in Fig. 5, while Table 6 contains statistics for each class. Histograms in Fig. 5 show that the distribution of each class is not smooth; clearly this is not a foolproof method to split aerosols into separate species. In addition large particle size (and thus low Ångström exponent) desert dusts can be encountered in both near shore and mid-ocean basins. Each class, however, shows characteristics of specific aerosol types. The 'coastal' class tends to have high Ångström exponents and relatively more data with high AOTs. This agrees with the assumption that non-dust continental aerosols are more likely to be close to their source over land. 'Offshore' aerosols tend to have much lower AOTs and a lower range of Ångström exponents, as expected of maritime and dust aerosols. The 'mid-range' class exhibits characteristics of both the other classes. Values in Table 6 reinforce this, showing decreasing AOT 500 nm values, decreasing Ångström exponents, and flat AOT 870 nm values with each class farther from shore. The number of measurements in each landmass distance class is roughly equal, indicating that the SIMBIOS instrument pool sampled in regions both near and far from the shore.

4. Classification

The temporally and geographically irregular nature of our data must be accommodated prior to any serious analysis. Otherwise, data statistics represent the temporal/geographical sampling methods as much as the nature of aerosols themselves. Furthermore, the SIMBIOS surface sampling strategy to date has focused on coastal regions and high AOT aerosol events. A change in this strategy would alter the results of a macroscopic statistical analysis. To account for this non-uniform sampling, an unsupervised classification routine has been utilized to split the data into major groups independent of measurement specifics. The entire aerosol dataset is composed of several statistical populations of data, each corresponding to an aerosol type (such as desert dust, urban pollution, maritime sea salt, etc.). The overly spare and non-uniform sampling methods associated surface optical measurements at sea mean that the measured ratios of aerosol type cannot represent the

ratios of the world as a whole. We therefore separate the data into each of these populations so we can report population statistics that are not overly affected by sampling methods. This is done by identifying natural clusters in the data through an unsupervised classification routine, then grouping these clusters into a handful of aerosol classes. The validity of this classification is tested by performing a Kolmogorov–Smirnov (KS) test for goodness of fit to a normal data distribution for Ångström exponent or a log-normal data distribution for AOT for each class. If each class is closer to a normal or log-normal distribution than the data as a whole, we conclude that the class represents a single population of aerosol type, or at least several types with a single set of optical characteristics (AOT and Ångström exponent).

4.1. K-means classification

The K-means unsupervised classification technique (Duda & Hart, 1973; Everitt, 1993; Schott, 1997, implemented using Interactive Data Language (IDL) version 5.3, from Research Systems) was used to group the data into clusters of similar nature, each representing a different aerosol type. This technique begins by randomly selecting an initial number of multivariate
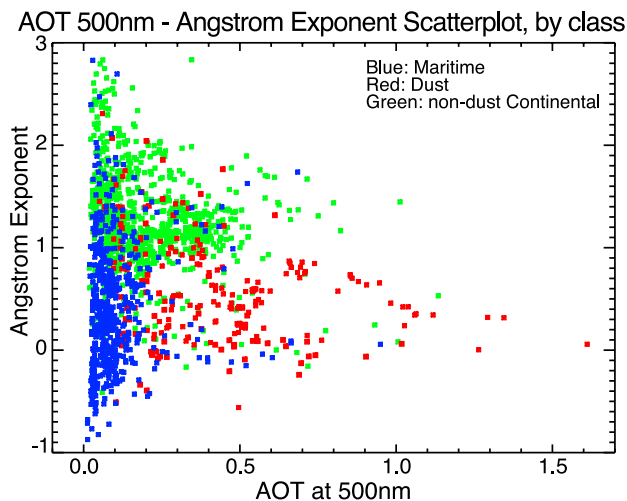

Fig. 6. Location on an AOT/Ångström exponent scatter plot of each class. Red data represent class 1 dust aerosols, while class 2 maritime aerosols are shown in blue. Green data points represent class 3 non-dust continental aerosols. (For interpretation of the references to colour in this figure legend, the reader is referred to the web version of this article.)

Table 8
Data split by class

Parameter	Mean	Median	STD	Distribution ratio
Entire binned dataset, 1715 data points				
AOT 500 nm	0.20	0.12	0.19	2.2
AOT 870 nm	0.13	0.08	0.15	
Ångström exponent	0.87	0.97	0.65	2.5
Class 1 dust, 237 data points				
AOT 500 nm	0.41	0.37	0.27	0.93
AOT 870 nm	0.32	0.26	0.25	
Ångström exponent	0.58	0.53	0.49	0.88
Class 2 maritime, 592 data points				
AOT 500 nm	0.10	0.08	0.09	0.99
AOT 870 nm	0.08	0.06	0.08	
Ångström exponent	0.42	0.34	0.59	0.89
Class 3 non-dust continental, 886 data points				
AOT 500 nm	0.21	0.17	0.15	2.7
AOT 870 nm	0.11	0.09	0.10	
Ångström exponent	1.3	1.2	0.47	3.4

Three parameters were used for our data classification: the natural logarithm of AOT at 500 nm ($\tau_a(500\text{ nm})$), Ångström exponent (α), and the natural logarithm of land distance. AOT in other bands were not used because spectral AOT values are highly correlated and their relationship is expressed by the Ångström exponent. Natural logarithms for AOT and land distance were used because the distribution of those data more closely resemble a log-normal than a normal distribution. The K-means classification technique assumes that input parameters are generally normally distributed. Natural logarithms of AOT and land distance were computed to convert those data distributions to a form closer to normally distributed than their natural state. To remove effects of scale, all three bands were normalized so their mean values are zero and unit is mean plus one standard deviation. Schott (1997) suggests splitting data into more classes than needed, and joining similar classes later, so our initial number of subclasses was 35. Subclasses were then grouped based

centers, $\mathbf{X}_j$, for each class j. $\mathbf{X}$ is presented in bold to indicate that it is a vector of spectral band centers. Data points are assigned to the class with the minimum distance, d_i, to $\mathbf{X}$:

$$d_{i,j} = \left[\left(\mathbf{X}_j - \mathbf{M}_i \right)^2 \right]^{1/2} \tag{15}$$

where $\mathbf{M}_i$ is the vector of values for data point i. Once a class has been found for each data point, class centers are recomputed as the average of all values of $\mathbf{M}$ within class j. This process is repeated iteratively until the re-computation of $\mathbf{X}$ yields little or no change. Once this has occurred, the final step uses the more sophisticated Mahalanobis distance computation for the final class assignment. The Mahalanobis distance, D_i, is:

$$D_{i,j} = \left(\mathbf{X}_j - \mathbf{M}_i \right)' \mathbf{S}_j^{-1} \left(\mathbf{X}_j - \mathbf{M}_j \right) \tag{16}$$

where $(\mathbf{X}_j - \mathbf{M}_i)'$ is the transposed $(\mathbf{X}_j - \mathbf{M}_i)$ and $\mathbf{S}_j^{-1}$ is the inverse of the covariance matrix for class j. The covariance matrix, $\mathbf{S}_j$, is computed:

$$\mathbf{S}_j = \begin{pmatrix} \sigma_{j11} & \sigma_{j12} & \cdots & \sigma_{j1q} \\ \sigma_{j21} & \ddots & & \\ \vdots & & & \\ \sigma_{jq1} & & & \sigma_{jqq} \end{pmatrix} \tag{17}$$

where q is the number of classification parameters and σ_{jxy} is the covariance for parameters x and y in class j. It is computed:

$$\sigma_{jxy} = \sum_{i=1}^{N} \frac{\left(M_{jx}(i) - M_{\text{mean } jx} \right)\left(M_{jy}(i) - M_{\text{mean } jy} \right)}{N - 1} \tag{18}$$

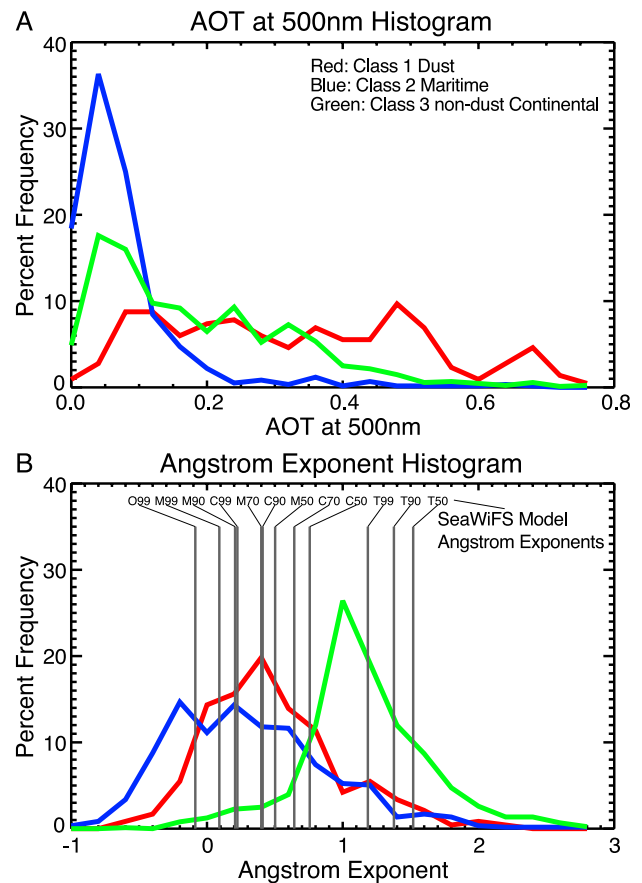where N is the number of data points within class j.

Fig. 7. Histograms of AOT at 500 nm and Ångström exponent for classified aerosol data. Class 1 dust aerosols are presented in red, class 2 maritime aerosols in blue, and class 3 non-dust continental aerosols in green. Bin sizes used in histogram computation were 0.04 for AOT at 500 nm (A) and 0.2 for Ångström exponent (B). Vertical black bars on the Ångström exponent histogram show the equivalent Ångström exponents for SeaWiFS aerosol models (Shettle & Fenn, 1979; Wang, 2000). (For interpretation of the references to colour in this figure legend, the reader is referred to the web version of this article.)

Table 9
Class 1 and maritime AERONET Cimel statistics

Parameter	Mean	Mode	STD
SIMBIOS class 2 maritime aerosols, 592 data points			
AOT 500 nm	0.10	0.08	0.09
Ångström exponent	0.42	0.25	0.59
AERONET Lanai site[a], Pacific Ocean, 722 data points			
AOT 500 nm	0.07	0.06	0.05
Ångström exponent	0.76	0.70	0.37
AERONET Nauru site[a], Pacific Ocean, 276 data points			
AOT 500 nm	0.08	0.06	0.03
Ångström exponent	0.43	0.30	0.35
AERONET Tahiti site[a], Pacific Ocean, 234 data points			
AOT 500 nm	0.07	0.06	0.02
Ångström exponent	0.74	0.70	0.27
AERONET Bermuda site[a], Atlantic Ocean, 590 data points			
AOT 500 nm	0.14	0.09	0.09
Ångström exponent	0.93	0.90	0.41
AERONET Ascension site[a], Atlantic Ocean, 338 data points			
AOT 500 nm	0.13	0.11	0.07
Ångström exponent	0.62	0.70	0.30

[a] AERONET data from Smirnov et al. (2002).

upon the location of their class centers, X_j. Table 7 lists boundaries for X that were used to create the final three classes. Classes whose centers, X_j, fall within these ranges are grouped into one of three final classes. Although these boundaries are somewhat arbitrary, actual data values extend beyond boundary ranges.

Boundaries between each class were chosen so that they roughly correspond to major aerosol types (Dubovik et al., 2002). Class 1 is meant to encompass desert dust, which has large particle sizes (thus, low α values). Aerosol optical thicknesses tend to be large when they are dominated by dust, so this class incorporates subclasses with high τ_a. Class 2 is meant to represent maritime, sea salt aerosols, which typically have large particle sizes (and thus low α) and occur in optically low magnitudes. Class 3 is meant to encompass all other aerosol types. This includes non-dust continental aerosols such as urban pollution. As shown in Appendix A, Ångström exponent uncertainties become very large as AOT values decrease, so forgiving upper and lower Ångström exponent bounds were set for low AOT classes (1 and 4).

4.2. Classification results and verification

Final classification results are shown in a τ_a–α scatter plot in Fig. 6, histograms in 7, and tabulated in Table 8. Results in Fig. 6 roughly follow major data clusters shown in Fig. 4. Fig. 7 shows unimodal histograms, indicating that classification has successfully split the data into unique populations.

Identifying each class as definitively belonging to and containing a specific aerosol type is difficult without performing a trajectory analysis, beyond the scope of this paper considering the number of data points involved. The classification approach is an attempt to both glean all possible aerosol information from the data and to remove the effects of non-uniform spatial and temporal distribution. This approach has its drawbacks, but we attempt to prove each class represents a single population of aerosols by testing the frequency distribution of AOTs and Ångström exponents. O'Neill et al. (2000) and Ignatov and Stowe (2002) show that populations of AOTs are distributed lognormally and Ångström exponents normally. Unlike this study, each used data with relatively regular spatial and temporal distributions. O'Neill et al. (2000) analyzed AERONET sun photometer measurements, while Ignatov and Stowe (2002) examined aerosol retrievals from AVHRR. We perform tests of AOT and Ångström exponent frequency distributions for the entire dataset, then compare results of the tests to the same for each class of data determined in the previous section. If the class frequency distribution test passes while the entire dataset fails, we can be confident that each class represents a single data population. If that is the case, we can be confident it is independent of spatial and temporal distribution and appropriate for analysis.

The KS test for goodness of fit (Sokal & Rohlf, 1995) was used to prove the hypothesis that our classified data are lognormally (for AOT) or normally (for the Ångström exponent) distributed. The KS test examines difference between a pair of cumulative relative frequency distributions. In this case, we test that our data distribution (f) matches a Gaussian normal distribution ($\hat{f}$). The following steps were used:

(1) Place the data in cumulative order;
(2) Standardize the data by setting the mean value to zero and mean plus one standard deviation to one. This is f;
(3) Compute the Gaussian normal distribution, $\hat{f}$, for the same number of data points;

Table 10
Characteristics of the 12 SeaWiFS aerosol models

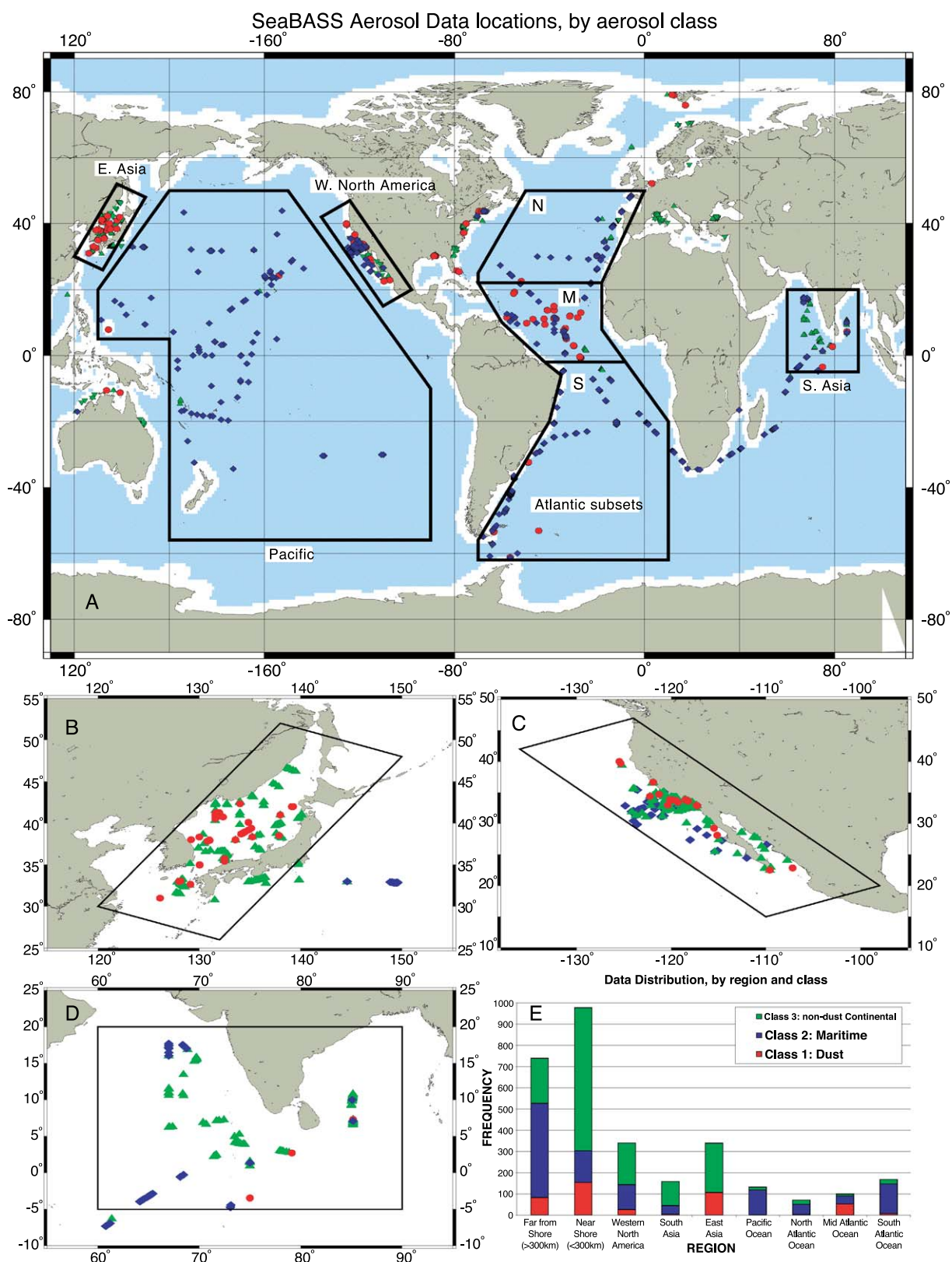| Aerosol model	Relative humidity (%)	Symbol	Ångström exponent	SSA, 865 nm
Oceanic	99	O99	−0.086	1.0
Maritime	50, 70, 90, 99	M50–M99	0.091–0.502	0.981–0.999
Coastal	50, 70, 90, 99	C50–C99	0.224–0.757	0.971–0.997
Tropospheric	50, 90, 99	T50–T99	1.185–1.519	0.930–0.987

Fig. 8. Global data distribution, by class. Class 1 dust aerosols data are in red, class 2 maritime aerosols are in blue and class 3 non-dust continental aerosols are in green. In part A, blue shaded regions are more than 300 km from the nearest major coast. Boxes in parts A–D show regions identified for more detailed analysis. Part E shows the quantity of data, by class, in each of these boxed regions.

Table 11
Classification results, by region

Parameter	AOT 500		Ångström exponent		Percentage
	Mean	Median	Mean	Median	
Entire dataset					
Class 1 dust	0.41	0.37	0.58	0.53	
Class 2 maritime	0.10	0.08	0.42	0.34	
Class 3 continental	0.21	0.17	1.26	1.20	
Far from shore	0.18	0.10	0.56	0.52	
Near shore	0.21	0.14	1.12	1.15	
W. North America					
All data	0.10	0.08	0.94	1.02	
Class 1 dust	0.17	0.12	0.69	0.67	8%
Class 2 maritime	0.08	0.06	0.59	0.64	34%
Class 3 continental	0.10	0.09	1.18	1.18	58%
North Atlantic					
All data	0.12	0.09	0.50	0.39	
Class 2 maritime	0.11	0.08	0.33	0.28	69%
Class 3 continental	0.13	0.14	0.92	1.00	27%
Mid-Atlantic					
All data	0.29	0.25	0.22	0.15	
Class 1 dust	0.35	0.33	0.19	0.16	52%
Class 2 maritime	0.20	0.14	0.08	0.09	38%
Class 3 continental	0.31	0.30	0.93	1.15	10%
South Atlantic					
All data	0.09	0.08	0.28	0.11	
Class 1 dust	0.18	0.22	0.20	0.11	5%
Class 2 maritime	0.08	0.06	0.19	0.01	83%
Class 3 continental	0.16	0.18	0.89	0.86	13%
Pacific					
All data	0.10	0.08	0.45	0.55	
Class 2 maritime	0.09	0.08	0.42	0.52	89%
Class 3 continental	0.13	0.08	0.81	0.79	10%
South Asia					
All data	0.28	0.32	1.00	1.09	
Class 2 maritime	0.14	0.10	0.66	0.65	26%
Class 3 continental	0.33	0.35	1.11	1.11	72%
East Asia					
All data	0.36	0.30	1.05	1.09	
Class 1 dust	0.54	0.51	0.65	0.61	31%
Class 3 continental	0.28	0.26	1.23	1.17	69%

(4) Find the largest difference between individual values of f and $\hat{f}$, and divide it by the number of data points, n. This is the KS test statistic, g_t;

(5) The KS critical value, g_c, is computed as $g_c = \frac{1.0427}{\sqrt{n}} - \frac{1}{2n}$,

(6) If g_t is less than g_c, the data are normally (for Ångström exponent) or log-normally (for AOT) distributed.

The 'distribution ratio' column in Table 8 shows the results of the KS test for that particular class and data type. The value is a ratio of the test statistic g_t to the critical value, g_c. Values of one or less represent data that pass the frequency distribution test, while increasing values indicate greater and greater divergences from the log-normal or normal distributions. KS test distribution ratios for the entire dataset are above 2.0, while classes 1 and 2 pass the KS test for both AOT at 500 nm and Ångström exponent. Class 3, as the container for all data that do not fall into class 1 or 2, fails the KS test. Class 3 could be split into smaller, more specific classes, but that was not done here, as it is beyond the scope of this ocean color remote sensing validation.

Table 9 compares statistics of class 2 maritime data to that from AERONET Cimel sun photometer sites in the Pacific and Atlantic Oceans representing maritime conditions (from Smirnov et al., 2003). Results compare very favorably,
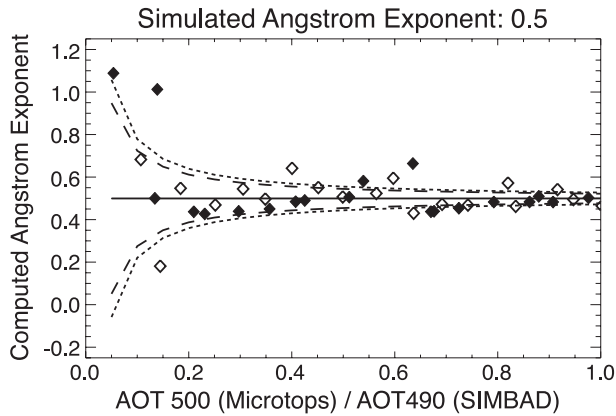
Simulated Angstrom Exponent: 0.5

Fig. A.1. Simulated values of τ_a were used to determine the relationship with α and $\Delta\alpha$. In this figure, the solid line represents the calculated value of α, dashed lines represent Microtops II $\alpha \pm \Delta\alpha$, dotted lines represent Simbad $\alpha \pm \Delta\alpha$, empty diamonds represent Microtops II α values computed when Gaussian random noise were added to the simulated τ_a, and filled diamonds represent the same for the Simbad. $\Delta\tau_a$ was computed using an airmass of 2.0. Simulations with other values of α show decreasing uncertainty as α diverges from zero.

especially in the Pacific Ocean, indicating that despite differences in instrument design and deployment, AERO-NET and SIMBIOS sun photometers yield similar measurements of aerosol optical properties. AERONET and SIMBIOS data are not, however, mutually exclusive. AERONET makes much more frequent measurements at fixed locations over an extended period of time, and can invert the data to yield aerosol particle size distributions. In contrast, SIMBIOS data are much less populous, do not include size distributions, but have the ability to measure in remote oceanic locations that AERONET cannot reach. These results help confirm that AERONET is successfully measuring maritime aerosol properties from island sites in the Pacific Ocean, and to a lesser degree, in the Atlantic Ocean.

5. Surface data compared to SeaWiFS aerosol models

Comparison and validation of aerosol products from ocean color sensors is one of the NASA SIMBIOS Project's main purposes for surface aerosol data (Wang et al, 2000). Validation is performed with the SeaWiFS aerosol models that are used for data processing to derive ocean color products. The primary goal of the SeaWiFS mission is routine measurements of global ocean color and ocean bio-optical properties. Atmospheric and surface effects must be removed from satellite measured radiances to retrieve ocean near-surface signals. This is known as atmospheric correction (Gordon & Wang, 1994). In the visible part of the spectrum, more than 90% of sensor-observed radiance is removed during atmospheric correction. The SeaWiFS atmospheric correction algorithm uses two NIR 40-nm wide bands (centered at 765 and 865 nm) to estimate the aerosol optical properties and extrapolate these into the visible spectrum where ocean color products are derived (Gordon & Wang, 1994). Aerosol models are needed for this process. The SeaWiFS 12 aerosol models are the Oceanic, Maritime, and Tropospheric models from Shettle and Fenn (1979), while Coastal models were introduced by Gordon and Wang (1994). Each model is modified by relative humidity, so the Oceanic model with the relative humidity (RH) of 99% is referred to as O99, the Maritime models with RH of 50%, 70%, 90%, and 99% as M50, M70, M90, and M99, the Coastal model with RH of 50%, 70%, 90%, and 99% as C50, C70, C90, and C99, and the Tropospheric model with RH of 50%, 90%, and 99% as T50, T90, and T99 (Wang, 2000). These aerosol models are all non- and weakly absorbing. Table 10 summarizes model optical properties. In Table 10, the Ångström exponent is the mean value for a given aerosol model, while the single scattering albedo (SSA) value is at a wavelength of 865 nm. The same
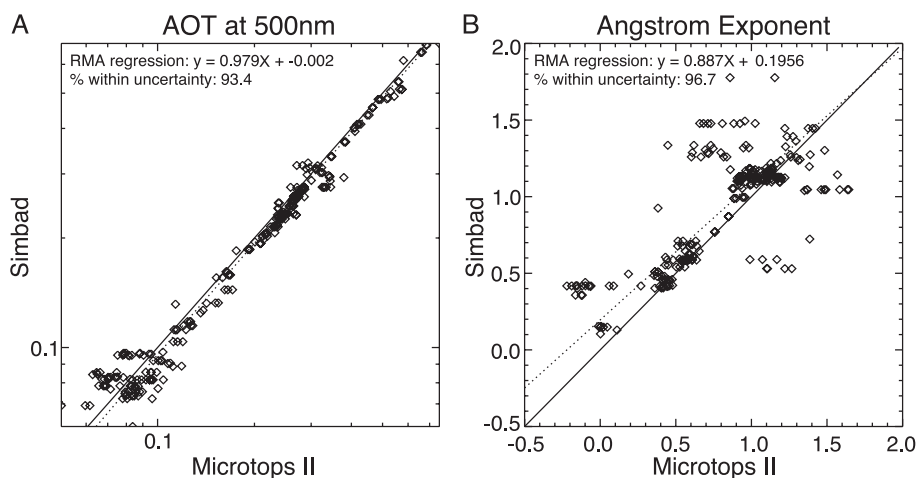

Fig. B.1. Comparison of concurrent measurements made with the Microtops II (abscissa) and SIMBAD (ordinate) sun photometers. Two hundred and seventy-four Microtops II and SIMBAD measurements fell within ±1 min, ±0.5 latitude, and ±0.5 longitude of each other, and are plotted above. The solid line shows the 1:1 relationship between values, while the dotted line is a reduced-major axis (RMA) regression between instruments. Note that both the plot and the RMA regression for AOT were performed in the log domain due to the log-normal distribution of these data.

Table B.1
Instrument comparison

Field (AOT or Ångström)	440	443	490	500	560	670	675	870	Ångström
% within uncertainty	87.9	95.6	92.7	93.4	89.0	81.7	89.7	82.4	96.7

atmospheric correction algorithm with a similar aerosol model set is also used for ocean color retrieval from NASA's Moderate Resolution Imaging Spectroradiometer (MODIS) (Esaias et al., 1998; Salomonson et al., 1989).

The aerosol model is defined by its particle size distribution and refractive indices (both real and imaginary parts). The Ångström exponent is related to the particle size distribution. Low Ångström exponent values indicate large particle sizes, while high values represent small aerosol particle sizes. For a given aerosol particle size distribution (aerosol model), the Ångström exponent is defined. Therefore, Ångström exponents from ground measurements can be used to indicate if an appropriate aerosol model set in terms of the particle size distribution is being used for SeaWiFS data processing. Note that, however, this only gives part of picture in terms of aerosol particle size distribution. To validate the aerosol model and give a complete picture, the refractive indices are also needed (Gross-Colzy et al., 2002). The refractive indices (or aerosol single-scattering albedo) can be derived with sky radiance measurements (Dubovik & King, 2000; Vermeulen et al., 2000; Wang & Gordon, 1993; Zhang & Gordon, 1997). Fig. 7B provides comparison results of the Ångström exponent from the SeaWiFS aerosol models with those of surface measurements. The Ångström exponent values for each aerosol model is represented as a vertical line. Ground-based sun photometer measurements of Ångström exponent obtained in the maritime environment are well represented with SeaWiFS aerosol models. Many Maritime aerosols have Ångström exponents lower than the SeaWiFS O99 model. The maritime aerosol Ångström exponent histogram width is partly due to measurement uncertainty, which is particularly large for low AOT maritime aerosols. An empirical test was performed to determine what portion of the Maritime aerosol Ångström exponent histogram width is due to uncertainty and which is geophysical. The histogram FWHM was measured as high uncertainty values were removed. The FWHM decreased linearly and was extrapolated to yield a value of about 0.70 with all uncertain data points removed. The mode of this histogram stayed constant at about 0.25. Therefore, FWHM values without error are −0.1 and 0.6, just within the range of SeaWiFS aerosol models.

6. Regional results

The main focus of this paper is a global analysis of the entire SeaBASS handheld sun photometer dataset. However, examining the classification results on a regional basis may have value. Seven regions around the globe were determined. Fig. 8 shows the geographical extent of these regions, along with enlarged views of three small regions and a plot with the class distribution in each region. In some cases, regions correspond to major study areas, such as the Western coast of North America (CalCOFI, IMECOCAL), East Asia/Sea of Japan (ACE-Asia) and South-West of the Indian Sub-continent (INDOEX). Other regions contain large oceanic basins, such as the Pacific Ocean region or each of the three Atlantic Ocean regions. Statistics associated with each region are in Table 11.
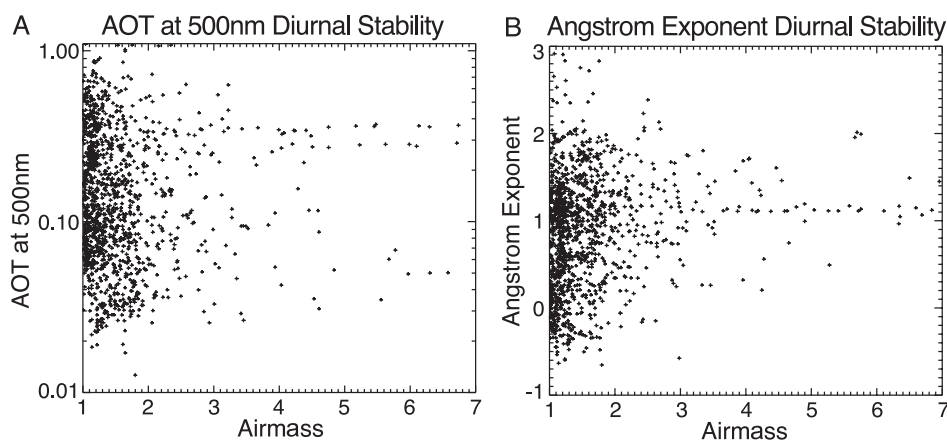

Fig. C.1. Relationship between airmass and AOT at 500 nm (A) and Ångström exponent (B). The correlation coefficients are 0.010 and 0.135, respectively. To account for log-normal distribution of AOT at 500 nm, the correlation was calculated with the logarithm of AOT values.

Table D.1
Data sources

Investigator(s)	Instrument	Institution	Experiment(s)	Cruise(s)	Dates	# data
R. Frouin	Simbad	Scripps Institution of Oceanography	IMECOCAL	IMECOCAL0201, -207, -301	2002/01/21–2003/02/15	46
R. Arnone	Microtops	Naval Research Laboratory	CoJet 7	Ocolor	2002/05/20–2002/05/24	105
W. Balch	Microtops	Bigelow Laboratory	Scotia Prince Ferry	s980911w, -17w, -18w, -29w; s981004w, -5w, -12w, -17w, -18w, -20w; el9907; s990523w; s990523w; s990605w, -6w; s990605w, -10w, -19w, -21w; s990802w, -10w, -23w, -24w; s990912w, -13w, -23w, -24w, -25w; s991008w, -12w, -16w; s000604w, s000702w, -11w, -12w; s000810w, -11w, -12w; s000914w, -30w;	1998/09/11–2000/09/30	327
A. Barnard, R. Letelier	Microtops	Oregon State University	MOCE	MOCE5	1999/10/01–1999/10/20	230
K. Carder	Microtops	University of South Florida	TOTO	tt0499	1999/04/14–1999/04/19	13
R. Frouin, P.-Y. Deschamps, D. Cutchin, P. Strutton, P. Flatau, B.G. Mitchell	Simbad	Scripps Institution of Oceanography, Université des Sciences et Technologies de Lille, Monterey Bay Aquarium Research Institute	MOKIHANA, INDEX, CALCOFI, MICRONESIAN, Sea of Japan, TOTO, VENICE, AMLR, ACE-ASIA, BILIM, P380108, POMME, KAIMIMOANA, OCEANIA	MOKIHANA0998, AEROSOLS99, BILIM9910, -0008, INDEX99 KAIMIMOANA0799, -0600, RB-01-02,IOFFE01, MICRONESIAN1098, OCEANIA1999, POMME01, tt0499, AMLR2000, AMLR2002, cal9807, -9, cal9901, -8, -10, cal0004, cal0007, -10, cal0101, -4, -7, -10, cal0204, WESPALIS2, Venice Tower, Nacre, SEAOFJAPAN0799, -0003	1998/07/18–2002/04/23	5105
D. Johnson	Microtops	Naval Research Laboratory	CoJet 5, 6	Pelican, cojet 6	2001/12/03–2002/3/05	328
K. Knobelspiesse	Microtops	NASA Goddard Space Flight Center	NORBAL, CALCOFI	norbal2002, cal0107	2001/07/10–2002/10/07	633
A. Magnuson, M. Mallonee, P.J. Werdell	Microtops	University of Maryland, NASA Goddard Space Flight Center	BIOCOMPLEXITY	bio0101	2001/04/04–2001/04/06	160
Majewski	Simbad	Curtin University of Technology	LB02	R/V Lady Basten	2002/06/06–2002/06/11	13
K. Markowicz, P. Flatau	Microtops	Scripps Institution of Oceanography	INDOEX	INDOEX99	1999/02/26–1999/03/30	779
M. Miller, M. Reynolds	Microtops	Brookhaven National Laboratory	Aerosol99	Aerosol99	1999/01/17–1999/02/06	528
S. Pegau	Microtops	Oregon State University	GOCAL	GOCAL99B	1999/10/29–1999/11/03	22
A. Subramaniam	Microtops, Simbad	Univeristy of Maryland	trichonesia, BRAZIL, MANTRA PIRANA, NOAA CSC, Searcher, trichototo, MASS BAY	trichonesia99, mar03atl, JAN01SJ, JUN01KN, JUL01KN, JUL02PAC, wf022, JUL02MB, oct99mab, NOV98SAB, Searcher99, trichototo99	1998/03/26–2002/04/10	625
R. Frouin, B.G. Micthell	Simbad	Scripps Institution of Oceanography	CALCOFI	cal0207, cal0211	2002/07/02–2002/11/25	369
E.J. Welton	Microtops	NASA Goddard Space Flight Center	ACE ASIA	RB0102	2001/03/15–2001/04/20	932

7. Conclusions

The NASA SIMBIOS Project has been collecting, processing and archiving aerosol optical data from handheld sun photometers in maritime locations since 1997, and to date has collected nearly 11,000 individual measurements from 145 individual cruises. This paper describes methods used by the SIMBIOS Project to calibrate instruments, process their data, remove erroneous measurements, perform quality control, and archive the results.

Maps and statistical analysis of the dataset as a whole reveal that it is heavily dependent upon its spatial and temporal collection characteristics. While about a third of the data were captured more than 500 km from a major landmass, much of the data were collected in coastal North America, East Asia, and Europe. Likewise, frequency histograms of AOT and Ångström exponent show several peaks, indicating that several different populations of aerosols were measured.

To remove data collection characteristics from an overall analysis, a semi-empirical K-means unsupervised classification technique was used to separate the data into optically unique populations. This was validated by proving (with the KS goodness of fit test) that individual classes are more likely to be log-normally (for AOT) or normally (for Ångström exponents) distributed than the dataset as a whole. This proof also reinforces the claim by several others (Ignatov & Stowe, 2002; O'Neill et al., 2000) that AOT values are log-normally distributed and should be treated appropriately.

Finally, properties for each class were presented, along with the characteristics of each class by regional oceanic basin. Ångström exponents from class 2 maritime data compare well with SeaWiFS aerosol models, and favorably with maritime aerosols measured by land-based AERONET Cimels in island sites. This further validates the SIMBIOS sun photometer dataset, which is calibrated with respect to AERONET Cimels. It is important to note, however, that a definitive comparison between Ångström exponents from maritime aerosols is difficult due to the large uncertainties associated with computing Ångström exponents in low aerosol optical thicknesses. In any case, the dataset adds to the scientific body of knowledge by extending sampling to previously remote maritime regions.

News and updates about the SIMBIOS sun photometer instrument pool can be found at http://simbios.gsfc.nasa.gov/Sunphotometers.

SIMBIOS data are available, with some restrictions, at http://seabass.gsfc.nasa.gov.

Acknowledgement

Appendix A. Ångström exponent computation

The Ångström exponent computation method used in this paper and by the SIMBIOS Project differs from the more common natural logarithm band ratio method. Rather than only using pairs of τ_a to determine the Ångström exponent, all available τ_a's are utilized. This is intended to reduce the effect of τ_a uncertainty on the Ångström exponent, while accounting for the variety of τ_a spectral bands in our instruments. The approach uses a non-linear, least squares, iterative fit to all available optical values of τ_a to Eq. (12). For the purposes of fitting, Eq. (12) is expressed as the geometric model:

$$y = ax^b \tag{A.1}$$

where paired values of x and y (λ and $\tau_a(\lambda)$, respectively) are fit using parameters $a = \tau_{a0}$ and $b = -\alpha$. Initial estimates of a for iteration are set to the τ_a from the longest available wavelength, while estimates for b are computed using an average value of α from Eq. (13) for all spectrally adjacent pairs of τ_a. $\Delta\tau_a$ values, computed as in Section 2.4, are used to create weights for each τ_a used in the fit. The fitting routine returns the fitted value (in our case, α) and the total error of that fit to the data. Because error based weights were used with input values of τ_a, the total fit error can be used as the uncertainty in α. Therefore, $\Delta\alpha$ expresses both the uncertainty associated with individual values of $\tau_a(\lambda)$ and deviation from Eq. (13). Data are removed if they have very large $\Delta\alpha$ values and thus do not fit the Junge Lawang (Ångström, 1929) and cannot be expressed with an Ångström exponent.

Fig. A.1 expresses the relationship between τ_a and $\Delta\alpha$. Data were synthesized for τ_a (500 nm) between 0.0 and 1.0 so that τ_a values at other wavelengths conform to a uniform Ångström exponent. α and $\Delta\alpha$ were then calculated using the fitting method shown above. Next, Gaussian random noise with a mean of zero and a standard deviation equal to $\Delta\tau_a$ were added to the synthesized τ_a values and α was recomputed. The scatter in the recomputed α values corresponds with $\Delta\alpha$, indicating that it is an appropriate measure of the uncertainty of α. Fig. A.1 also illustrates the

non-uniform nature of $\Delta\alpha$ with respect to τ_a. Indeed, α becomes dominated by uncertainty when τ_a is less than 0.1 and $\Delta\tau_a$ exceeds the absolute value of τ_a.

Appendix B. Instrumental differences

To ensure the SIMBIOS Instrument Pool dataset continuity, a comparison between concurrent measurements was performed. Two hundred and seventy-four Microtops II and SIMBAD measurements fell within ±1 min, ±0.5 latitude, and ±0.5 longitude of each other (measured from the same ship). Fig. B.1 contains scatter plots of these data for AOT at 500 nm (Fig. B.1A) and Ångström exponent (Fig. B.1B). The AOT 500-nm relationship is well behaved, with minimal scatter and a reduced-major axis (RMA) regression slope of 0.979. 93.4% of the data fall within uncertainty values. The Ångström exponent relationship shows considerably more scatter, although 96.7% of the data fall within the (relatively large) uncertainty values. The RMA regression slope for Ångström exponent is 0.887. A comparison between all bands is presented in Table B.1. The vast majority of AOT and Ångström exponent data fall within uncertainty values of each other, and have a relationship without significant biases or trends.

Appendix C. Diurnal stability

AOTs and Ångström exponents from the SIMBIOS Instrument Pool should be independent of measuring geometry and time. To test this, airmass values from each measurement were plotted against AOT at 500 nm and Ångström exponent. Fig. C.1 shows these plots. The correlation coefficient for the airmass vs. logarithm of AOT at 500 nm (Fig. C.1A) is 0.010, indicating a negligible linear relationship. The relationship between airmass and Ångström exponent (Fig. C.1B) is somewhat larger, with a value of 0.135. Due to the higher uncertainty associated with the Ångström exponent, this value can also be associated with a negligible linear relationship. Therefore, there is no indication of the type of calibration errors that may be shown with a relationship between AOT, Ångström exponent and airmass.

References

Ångström, Å. (1929). On the atmospheric transmission of sun radiation and on dust in the air. *Geografos Annale Deutsche*, *11*, 156–166.

Everitt, B. (1993). *Cluster analysis* (Third edition). New York: Halsted Press.

Campbell, J. W. (1995). The lognormal distribution as a model for bio-optical variability in the sea. *Journal of Geophysical Research*, *100*(C7), 13237–13254.

Deschamps, P. -Y., Fougnie, B., Frouin, R., Lecomte, P., & Verwaerde, C. (2004). SIMBAD: A field radiometer for satellite ocean—Color validation. *Applied Optics*, *43*, 4055–4069.

Dubovik, O., & King, M. (2000). A flexible inversion algorithm for retrieval of aerosol optical properties from Sun and sky radiance measurements. *Journal of Geophysical Research*, *105*, 20673–20696.

Dubovik, O., Holben, B. N., Eck, T. F., Smirnov, A., Kaufman, Y. J., King, M. D., et al. (2002). Variability of absorption and optical properties of key aerosol types observed in worldwide locations. *Journal of the Atmospheric Sciences*, *59*, 590–608.

Duda, R. O., & Hart, P. E. (1973). *Pattern classification and scene analysis*. New York: John Wiley and Sons.

Eck, T. F., Holben, B. N., Reid, J. S., Dubovik, O., Smirnov, A., O'Neill, N. T., et al. (1999). Wavelength dependence of the optical depth of biomass burning, urban, and desert dust aerosols. *Journal of Geophysical Research*, *104*(D24), 31333–31349.

Esaias, W. E., Abbott, M. R., Barton, I., Brown, O. B., Campbell, J. W., Carder, K. L., et al. (1998). An overview of MODIS capabilities for ocean science observations. *IEEE Transactions on Geoscience and Remote Sensing*, *36*, 1250–1265.

Fargion, G. S., & McClain, C. R. (2003). SIMBIOS Project 2002 Annual Report, NASA Tech. Memo. 2003-211622, NASA Goddard Space Flight Center, Greenbelt, MD.

Fargion, G. S., & Mueller, J. L. (2000). Ocean Optics Protocols for Satellite Ocean Color Sensor Validation: Revision 2. *NASA Tech. Memo. 2000-209966*, Eds., NASA Goddard Space Flight Center, Greenbelt, MD.

Fargion, G. S., Barnes, R., & McClain, C. (2001). In Situ Aerosol Optical Thickness Collected by the SIMBIOS Program (1997–2000): Protocols, and Data QC and Analysis. *NASA Tech. Memo. 2001-209982*, Eds., NASA Goddard Space Flight Center, Greenbelt, MD.

Gordon, H. R., & Wang, M. (1994). Retrieval of water-leaving radiance and aerosol optical thickness over the oceans with SeaWiFS: A preliminary algorithm. *Applied Optics*, *33*, 443–452.

Gross-Colzy, L., Frouin, R., Pietras, C., & Fargion, G. (2002). Non-supervised classification of aerosol mixtures for ocean color remote sensing. In R. Frouin, Y. Yuan, & H. Kawamura (Eds.), *Proceedings of SPIE Vol. 4892, Ocean Remote Sensing and Applications* (pp. 95–104). Bellingham: SPIE.

Holben, B. N., Eck, T. F., Slutsker, I., Tanre, D., Buis, J. P., Setzer, A., et al. (1998). AERONET—A federated instrument network and data archive for aerosol characterization. *Remote Sensing of Environment*, *66*, 1–16.

Ichoku, C., Levy, R., Kaufman, Y. J., Remer, L. A., Li, R. -R., Martins, V. J., et al. (2002). Analysis of the performance characteristics of the five-channel microtops II sun photometer for measuring aerosol optical thickness and precipitable water vapor. *Journal of Geophysical Research*, *107*(D13), Art No. 4179.

Ignatov, A., & Stowe, L. (2002). Aerosol retrievals from individual AVHRR channels: Part II. Quality control, probability distribution functions, information content, and consistency checks of retrievals. *Journal of the Atmospheric Sciences*, *59*, 335–362.

Iqbal, M. (1983). *An introduction to solar radiation* (pp. 390). San Diego, CA: Academic Press.

Kasten, F., & Young, A. T. (1989). Revised optical airmass tables, an approximation formula. *Applied Optics*, *28*, 4735–4738.

Knobelspiesse, K. D., Pietras, C., & Fargion, G. S. (2003). Sun-pointing error correction for sea deployment of the MICROTOPS II handheld sun photometer. *Journal of Atmospheric and Oceanic Technology*, *20*, 767–771.

Komhyr, W. D., Grass, R. D., & Leonard, R. K. (1989). Dobson spectrophotometer 83: A standard for total ozone measurements, 1962–1987. *Journal of Geophysical Research*, *94*, 9847–9861.

Morys, M., Mims III, F. M., Hagerup, S., Anderson, S. E., Baker, A., Kia, J., et al. (2001). Design, calibration and performance of MICROTOPS II handheld ozone monitor and sun photometer. *Journal of Geophysical Research*, *106-D13*, 14573–14582.

Mueller, J. L., & Fargion, G. S. (2002a). Ocean Optics Protocols for Satellite Ocean Color Sensor Validation, Revision 3, Volume I. *NASA Tech. Memo. 2002-210004/Rev3-Vol1*, NASA Goddard Space Flight Center, Greenbelt, MD.

Mueller, J. L., & Fargion, G. S. (2002b). Ocean Optics Protocols for Satellite Ocean Color Sensor Validation, Revision 3, Volume II. *NASA Tech. Memo. 2002-210004/Rev3-Vol2*, NASA Goddard Space Flight Center, Greenbelt, MD.

Mueller, J. L., Fargion, G. S., & McClain, C. R. (2003a). Ocean Optics Protocols For Satellite Ocean Color Sensor Validation, Revision 4, Volume I. *NASA Tech. Memo. 2003-21621/Rev-Vol1*, NASA Goddard Space Flight Center, Greenbelt, MD.

Mueller, J. L., Fargion, G. S., & McClain, C. R., (2003b). Ocean Optics Protocols For Satellite Ocean Color Sensor Validation, Revision 4, Volume II. *NASA Tech. Memo. 2003-21621/Rev-Vol2*, NASA Goddard Space Flight Center, Greenbelt, MD.

Mueller, J. L., Fargion, G. S., & McClain, C. R. (2003c). Ocean Optics Protocols For Satellite Ocean Color Sensor Validation, Revision 4, Volume III. *NASA Tech. Memo. 2003-21621/Rev-Vol3*, NASA Goddard Space Flight Center, Greenbelt, MD.

Nicolet, M. (1981). The solar spectral irradiance and its action in the atmospheric photodissociation process. *Planetary and Space Science*, *29*, 951–974.

O'Neill, N., & Royer, A. (1993). Extraction of biomodal aerosol-size distribution radii from spectral and angular slope (Angstrom) coefficients. *Applied Optics*, *32*(9), 1642–1645.

O'Neill, N. T., Ignatov, A., Holben, B. N., & Eck, T. F. (2000). The lognormal distribution as a reference for reporting aerosol optical depth statistics; empirical tests using multi-year, multi-site AERONET sunphotometer data. *Geophysical Research Letters*, *20*, 3333–3336.

Porter, J. N., Miller, M., Pietras, C., & Motell, C. (2001). Ship-based sun photometer measurements using microtops sun photometers. *Journal of atmospheric and oceanic technology*, *18*, 765–774.

Russell, P. B., Livingston, J. M., Dutton, E. G., Pueschel, R. F., Reagan, J. A., DeFoor, T. E., et al. (1993). Pinatubo and Pre-Pinatubo optical-depth spectra: Mauna Loa measurements, comparisons, inferred particle size distributions, radiative effects and relationships to Lidar data. *Journal of Geophysical Research*, *98*(D12), 22969–22985.

Salomonson, V. V., Barnes, W. L., Maymon, P. W., Montgomery, H. E., & Ostrow, H. (1989). MODIS: Advanced facility instrument for studies of the Earth as a system. *IEEE Transactions on Geoscience and Remote Sensing*, *27*, 145–152.

Schott, J. R. (1997). *Remote sensing: The image chain approach* (pp. 52–62). New York: Oxford University Press.

Shettle, E. P., & Fenn, R. W. (1979). Models for the aerosols of the lower atmosphere and the effects of humidity variations on their optical properties. *AFGL Tech. Rep.*, AFGL-TR-79-0214.

Smirnov, A., Holben, B. N., Kaufman, Y. J., Dubovik, O., Eck, T. F., Slutsker, I., et al. (2002). Optical properties of atmospheric aerosol in maritime environments. *Journal of the Atmospheric Sciences*, *59*, 501–523.

Smirnov, A., Holben, B. N., Dubovik, O., Frouin, R., Eck, T. F., & Slutsker, I. (2003). Maritime component in aerosol optical models derived from Aerosol Robotic Network data. *Journal of Geophysical Research*, *108*(D1), 4033.

Sokal, R. R., & Rohlf, F. J. (1995). Biometry: The principles and practice of statistics in biological research. (Third edition)San Francisco, CA: W.H. Freeman and Company.

Vermeulen, A., Devaux, C., & Herman, M. (2000). Retrieval of the scattering and microphysical properties of aerosols from ground-based optical measurements including polarization: I. Method. *Applied Optics*, *39*, 6207–6220.

Wang, M. (2000). The SeaWiFS atmospheric correction algorithm updates. S. B. Hooker, & E. R. Firestone *NASA Tech. Memo. 2000-206892, SeaWiFS Post Launch Technical Report Series, vol. 9*. (pp. 57–63). Greenbelt, MD: NASA Goddard Space Flight Center.

Wang, M., & Gordon, H. R. (1993). Retrieval of the columnar aerosol phase function and single scattering albedo from sky radiance over the ocean: Simulations. *Applied Optics*, *32*, 4598–4609.

Wang, M., Bailey, S., & McClain, C. R. (2000). SeaWiFS Provides Unique Global Aerosol Optical Property Data. *Eos Transactions* (pp. 197). American Geophysical Union.

Werdell, P. J., & Bailey, S. W. (2002). The SeaWiFS Bio-Optical Archive and Storage System (SeaBASS): Current Architecture and Implementation, *NASA Tech. Memo. 2002-211617*. NASA Goddard Space Flight Center, Greenbelt, MD.

Zhang, T., & Gordon, H. R. (1997). Retrieval of elements of the columnar aerosol scattering phase matrix from polarized sky radiance over the ocean: Simulations. *Applied Optics*, *36*, 7948–7959.